Landslides (2007) 4:357–369
DOI 10.1007/s10346-007-0092-1
Received: 24 December 2006
Accepted: 20 August 2007

Yasuhiko Okada · Hirotaka Ochiai

Coupling pore-water pressure with distinct element method and steady state strengths in numerical triaxial compression tests under undrained conditions

Abstract The undrained shear behaviour of sands has been a key topic after the devastating geo-disasters during the 1964 Niigata Earthquake in Japan. Extensive geo-technical soil tests, especially undrained triaxial compression tests, have revealed that the liquefaction phenomenon was the major cause for the disaster expansions. To numerically reproduce the liquefaction phenomenon, the pore-water pressure was coupled with a distinct element method. In this model, the dynamic changes in pore-water pressure were taken into consideration by the changes in volumetric strain and modulus of compressibility of water in the respective measurement spheres. Fluid-flows among the measurement spheres were controlled by Darcy's law. The effective stress paths and steady state strengths in undrained triaxial compression tests associated with the wide ranges of initial void ratio were investigated. The effective mean stresses of medium-dense to dense numerical specimens at the steady state were negatively proportional to the initial void ratio. Loose numerical specimens reproduced quasi-liquefaction with the effective mean stresses that were less than 25% of the initial value. The medium-dense numerical specimens reproduced the phase transformation that was a typical characteristic of granular materials. The rolling restraints did not much influence of the effective angle of internal friction but strongly affected pore-water pressure behaviour within a certain range of initial void ratio.

Keywords Fluid-coupling · Distinct element method · Pore-water pressure · Steady state strengths

Introduction

The liquefaction behaviours of sands have received a considerable amount of attention after it was revealed that the liquefaction was the major triggering factor of the devastating geo-disasters in the 1964 Niigata Earthquake in Japan (Seed and Lee 1966; Yoshimi et al. 1977; Seed 1979; Finn 1981; Ishihara 1993). Because flow-type landslides are strongly associated with the liquefaction phenomenon (Sassa 1988; Ishihara et al. 1990; Eckersley 1985), the extensive geo-technical soil tests, especially the undrained triaxial compression tests, have been performed under both dynamic stress-loading and static conditions (Casagrande 1971; Castro and Poulos 1977), and it was concluded that the collapse of loose meta-stable structures due to the compressive deformation produced excessive pore-water pressure resulting in the liquefaction (Hutchinson 1986). Because the triaxial compression tests cannot investigate the undrained shear behaviour subjected to large shear displacement, the studies using the ring-type direct shear testing apparatus have also been conducted. Sassa (1996) and Sassa et al. (1996) proposed the sliding surface liquefaction that occurred within the shear zone where soil particles were crushed and comminuted. The point to note is that the sliding surface liquefaction takes place even when the specimens are medium-dense through dense, whereas the liquefaction could only occur in the loose specimens. Okada et al. (2004) stated that the crushed and comminuted particles could form the less-permeable shear zone, and it hindered the dissipation of generated excessive pore-water pressure in the ring shear tests. Iverson and LaHussen (1989) examined the changes in the down slope displacement of the soil layer surface and pore-water pressure in the landslide experiments using quasi-real scale-model slope. They insisted that the generation of excessive pore-water pressure was due to the contractive volumetric deformation subjected to shearing when the soil mass moved down slope, and this fact was in good agreement with the liquefaction theory by Casagrande (1971) and Castro and Poulos (1977) found in the undrained triaxial compression tests.

The numerical simulations for the studies of landslide mechanisms have also been developed, as well as the geo-technical soil tests and model-slope tests. Cundall and Strack (1979) proposed a discrete numerical method, i.e. distinct element method, to model the shear behaviour of granular assemblies. In distinct element method, the contacts between ball and ball (in three dimensions) or disc and disc (in two dimensions) are modeled by the mechanical elements of elastic spring and viscous damper (Fig. 1). Kiyama and Fujimura (1983) numerically simulated the gravity flow of rock-like granular materials by two-dimensional distinct element method. Tarumi and Hakuno (1987) applied the two-dimensional distinct element method to the rock avalanches and debris flows explaining the mechanisms of large rocks' floating-up to the flow surface and the subsequent aggregations to the front of the surge. Although the distinct element method has difficulties in tuning up the setting parameters and it consumes rather too much time with limited number of elements, it is a very strong tool for the investigation of the phenomena, which have the characteristics of uncontinuum (Hakuno 1997). Okura et al. (1994) employed the two-dimensional distinct element method for the movement of the soils packed in the quasi-real scale-model slope, in which a slope failure occurred by the artificial rainfall. However, their investigations were conducted in two dimensions and did not take the excess pore-water pressure into consideration.

As for the simulations by distinct element method of the geo-technical soil tests, Kiyama et al. (1994) and Tarumi and Hakuno (1987) investigated the generation of excessive pore-water pressure under undrained conditions; however, they were in two dimensions. Ng and Dobry (1994) employed a three-dimensional distinct element method investigating the reduction in effective normal stress under the constant volume conditions as the equivalents of the excessive pore-water pressure generation under undrained conditions. Hakuno and Tarumi (1988) pointed out that for the liquefaction studies, three-dimensional distinct element method was necessary because the degree of freedom for the particle movements in two dimensions was not sufficient. In light of these mentioned, the authors have performed the numerical simulations

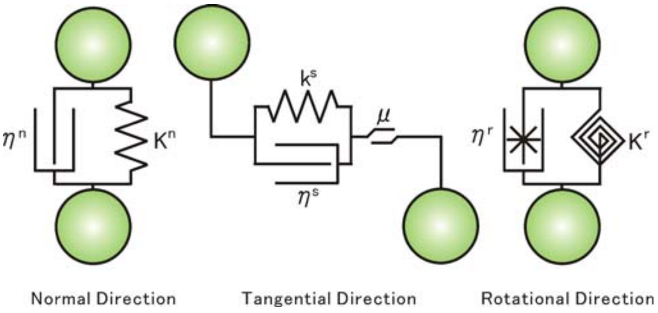

Fig. 1 Mechanical elements introduced in ball–ball contacts in normal, tangential and rotational directions in distinct element method

of the undrained triaxial compression tests by coupling the pore-water pressure with three-dimensional distinct element method focusing on the changes in the excessive pore-water pressure under undrained conditions as the key basic studies for the elucidation of fluidisation mechanisms of the flow-type landslides (Okura et al. 2004; Okada and Ochiai 2006). In this study, the viscous damping was substituted for the local damping (Cundall 1989) to keep Newton's second law of motion. Furthermore, the restriction of rolling movements of the ball elements were modeled and introduced in the calculation scheme, and the pore-water pressure and shear strengths in the undrained triaxial compression tests were examined.

Finally, it should be mentioned that the points of this paper are to introduce the method of coupling the pore-water pressure in three-dimensional distinct element method and to derive some knowledge by using this new model. The ball number used in this simulation was less than 500; this might not be ideal to reproduce the essential behaviours of granular assemblage such as the development of shear banding or strain localisation. However, because the performance of PC is limited, in this paper, the numerical simulation of triaxial compression tests was conducted with around 500 ball elements in considering the simulation time needed for the calculations.

Procedure of numerical calculation

The detailed procedure of the fluid-coupled distinct element method is highlighted. First, the measurement sphere, which assigns the pore-water pressure is introduced, and then the calculation scheme is shown. The measurement sphere surrounds and coincides with the centre of each ball element with the radius R (Fig. 2). The radius of the measurement sphere is twice of that of the ball element, i.e. $2R$. The mean velocity and centre position of the ball and wall elements that intersect a given measurement sphere are calculated as follows:

$$\overline{\nu_i} = \frac{\sum_N \nu_i}{N}, \overline{\chi_i} = \frac{\sum_N \chi_i}{N} (i = 1,\ 2,\ 3) \tag{1}$$

in which N is the total number of ball and wall elements contained in the measurement sphere, ν_i is the translational velocity, and χ_i is centroid location of ball and wall elements. The relative velocity and position of ball and wall elements from the mean values are given by:

$$\widetilde{\nu_i} = \nu_i - \overline{\nu_i}, \widetilde{\chi_i} = \chi_i - \overline{\chi_i} (i = 1,\ 2,\ 3) \tag{2}$$

In this model, the relative velocity is estimated by using strain rate tensor $\dot{\beta}_{ij}$ expressed as:

$$\widetilde{\nu_i}' = \dot{\beta}_{ij}\widetilde{\chi_j}(i = 1,\ 2,\ 3) \tag{3}$$

The strain rate tensor $\dot{\beta}_{ij}$ that minimises the difference between relative velocity $(\widetilde{\nu_i})$ and the estimated relative velocity $(\widetilde{\nu_i}')$ is computed using the least square method, in which the following nine equations are resolved. In this calculation, LU decomposition based on the Crout's algorithm, and backward- and forward-substitutions were conducted.

$$\sum_N \dot{\beta}_{ik}\widetilde{\chi_k}\widetilde{\chi_j} = \sum_N \widetilde{\nu_i}\widetilde{\nu_j}(i,\ j = 1,\ 2,\ 3) \tag{4}$$

The volumetric strain during the increment of time, Δt is obtained like:

$$\varepsilon_\nu = \dot{\varepsilon}_\nu \Delta t = \left(\dot{\beta}_{11} + \dot{\beta}_{22} + \dot{\beta}_{33}\right)\Delta t \tag{5}$$

The changes in pore-water pressure due to the volume change is given by the product of volumetric strain and the modulus of compressibility of water, and it is applied as forces to the centres of ball and wall elements, which are within a given measurement sphere as follows:

$$F_{\text{ball}} = P'_{\text{A}}S = (P_{\text{A}} + \Delta P)S = (P_{\text{A}} + E_\nu\varepsilon_\nu)\pi r^2 \tag{6}$$

$$F_{\text{wall}} = P'_{\text{A}}S' = (P_{\text{A}} + \Delta P)S' = (P_{\text{A}} + E_\nu\varepsilon_\nu)\pi\{(2r)^2 - L^2\} \tag{7}$$

in which P_{A} is the pore-water pressure of the measurement sphere A, ΔP is incremental changes in pore-water pressure within Δt, S and S' are the areas on which pore-water pressure acts (Fig. 2), E_{w} is the modulus of compressibility of water. The fluid-flow due to the difference of pore-water pressure values between the neighbouring measurement spheres is given based on the Darcy's law by:

$$\Delta Q_{\text{AB}} = k \cdot \pi r^2 \frac{P'_{\text{B}} - P'_{\text{A}}}{\rho \cdot g \cdot L_{\text{AB}}}\Delta t \tag{8}$$

in which P_{A}' and P_{B}' are the pore-water pressure of the measurement spheres A and B, and g is the gravitational acceleration, L_{AB} is the distance between the measurement spheres A and B. The total changes in pore-water pressure (P_{A}) because of the fluid-flow is given by:

$$P_{\text{A}} = \sum_N \Delta P_{\text{AB}} = \sum_N \frac{E_\nu \Delta Q_{\text{AB}}}{V_{\text{A}}} \tag{9}$$

where V_{A} is the volume of the measurement sphere A.

The calculation scheme of the force transmissions between ball element A (position: $[\chi_{\text{A}}] = (\chi_{\text{A1},}\chi_{\text{A2},}\chi_{\text{A3}})$, angular velocity: $[\omega_{\text{A}}] = (\omega_{\text{A1},}\omega_{\text{A2},}\omega_{\text{A3}})$) and ball element B (position: $[\chi_{\text{B}}] = (\chi_{\text{B1},}\chi_{\text{B2},}\chi_{\text{B3}})$,

Fig. 2 Schematic illustration of measurement sphere and cross section areas

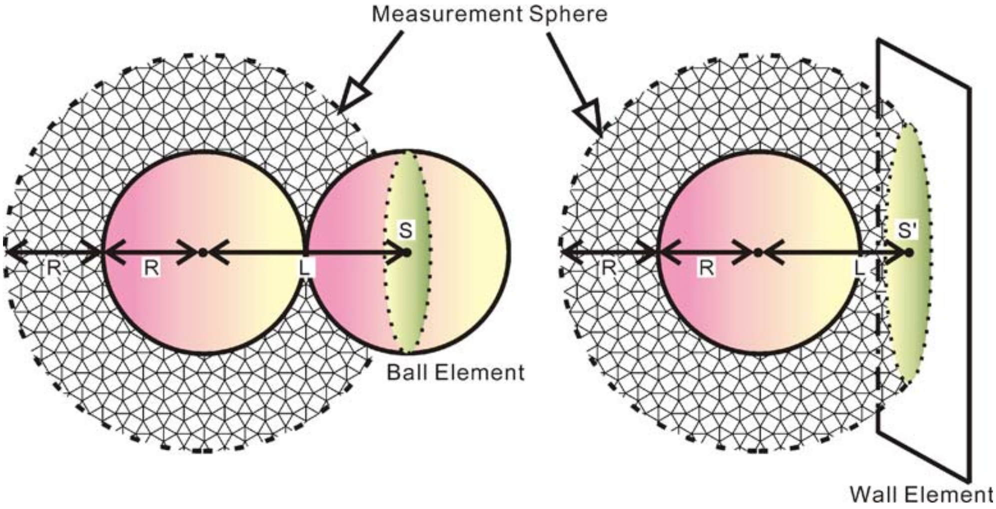

angular velocity: $[\omega_{\mathrm{B}}] = (\omega_{\mathrm{B}_1}\omega_{\mathrm{B}_2}\omega_{\mathrm{B}_3})$) are given below. When Eq. 10 is satisfied, it is judged that two ball elements are in contacts.

$$L_{\mathrm{AB}} = \sqrt{(\chi_{\mathrm{A}1}-\chi_{\mathrm{B}1})^2+(\chi_{\mathrm{A}2}-\chi_{\mathrm{B}2})^2+(\chi_{\mathrm{A}3}-\chi_{\mathrm{B}3})^2} \le r_{\mathrm{A}} + r_{\mathrm{B}} \tag{10}$$

in which L_{AB} is the distance between the two ball elements, r_{A} and r_{B} are the radius of ball elements A and B. The normal unit vector from the centre of ball element A to B is expressed as:

$$[n_i] = \frac{[\chi_{\mathrm{B}i}] - [\chi_{\mathrm{A}i}]}{\langle L_{\mathrm{AB}} \rangle} (i = 1,\ 2,\ 3) \tag{11}$$

The force by elastic spring and viscous dashpot are divided into normal and tangential directions like:

$$[\mathrm{E}_i] = [\mathrm{E}_i^n] + [\mathrm{E}_i^s] (i = 1,\ 2,\ 3) \tag{12}$$

$$[D_i] = [D_i^n] + [D_i^s] (i = 1,\ 2,\ 3) \tag{13}$$

The force by elastic spring in normal direction is given by the values proportional to the amount of intersection of two ball elements. The amount of intersection is expressed as:

$$\langle U^n \rangle = r_{\mathrm{A}} + r_{\mathrm{B}} - \langle L_{\mathrm{AB}} \rangle \tag{14}$$

hence, the force by elastic spring in normal direction is:

$$[\mathrm{E}_i^n] = K^n \langle U^n \rangle [n_i] (i = 1,\ 2,\ 3) \tag{15}$$

The viscous damping force in normal direction is:

$$[D_i^n] = \eta^n \frac{\langle \Delta U^n \rangle}{\Delta t} [\eta_i] (i = 1,\ 2,\ 3) \tag{16}$$

The contact point of two ball elements is expressed:

$$\left\langle \chi_i^{(c)} \right\rangle = [\chi_{\mathrm{A}i}] + \left(r_{\mathrm{A}} - \frac{1}{2} \langle U^n \rangle \right) [n_i] (i = 1,\ 2,\ 3) \tag{17}$$

The force by elastic spring in tangential direction is computed in an incremental fashion. The relative motion of contact (which defined the velocity of ball element B relative to A) is given by:

$$\begin{aligned} [\widehat{\nu}_i] &= \left[\dot{\chi}_{\mathrm{B}i}^{(c)} \right] - \left[\dot{\chi}_{\mathrm{A}i}^{(c)} \right] \\ &= \left\{ [\dot{\chi}_{\mathrm{B}i}] + \varepsilon_{ijk} [\omega_{\mathrm{B}j}] \left(\left[\chi_k^{(c)} \right] - [\chi_{\mathrm{B}k}] \right) \right\} \\ &\quad - \left\{ [\dot{\chi}_{\mathrm{A}i}] + \varepsilon_{ijk} [\omega_{\mathrm{A}j}] \left(\left[\chi_k^{(c)} \right] - [\chi_{\mathrm{A}k}] \right) \right\}^{(i=1,\ 2,\ 3)} \end{aligned} \tag{18}$$

in which ε_{ijk} is Eddington's epsilon and Einstein's summation convention is applied on subscript of *j* and *k*. Eddington's epsilon is defined as:

$$\varepsilon_{ijk} = \begin{cases} 0,\ \mathit{if},\ 2\ \mathit{indices\ coincide} \\ +1,\ \mathit{if}\ i,\ j,\ k\ \mathit{permute\ like}\ 1,\ 2,\ 3; \\ -1,\ \mathit{otherwise}. \end{cases} \tag{19}$$

The relative motion is also divided into normal and tangential directions. The relative motion in tangential direction is as follows:

$$[\widehat{\nu}_i^s] = [\widehat{\nu}_i] - [\widehat{\nu}_i^n] = [\widehat{\nu}_i] - [\widehat{\nu}_j].[n_j][n_i] (i = 1,\ 2,\ 3) \tag{20}$$

The incremental displacement in tangential direction is given by:

$$[\Delta U_i^s] = [\widehat{\nu}_i^s].\Delta t (i = 1,\ 2,\ 3) \tag{21}$$

Accordingly, the contact force by elastic spring in tangential direction due to this incremental displacement is:

$$[\Delta E_i^s] = k^s [\Delta U_i^s] (i = 1,\ 2,\ 3) \tag{22}$$

The additional force due to the changes in contact point during Δt is approximated by:

$$\begin{aligned} [E_i'^s] &= [E''^s{}_j] \{ \delta_{ij} - \varepsilon_{ijk} [\widetilde{\omega}_k] \Delta t \} \\ &= \left[\left\{ [E_m^s]_{\mathrm{old}} \left(\delta_{\mathrm{lm}} - \varepsilon_{\mathrm{lmn}} \varepsilon_{\mathrm{npq}} [n_{\mathrm{p}}]_{\mathrm{old}} [n_{\mathrm{q}}] \right) \right\}_j^s \right] \{ \delta_{ij} - \varepsilon_{ijk} [\widetilde{\omega}_k] \Delta t \}^{(i=1,\ 2,\ 3)} \end{aligned} \tag{23}$$

where δ is Kronecker's Delta, the subscription "old" signifies the values at the previous time-step, i.e. before the update, and $[\widetilde{\omega}_k]$ is the average of angular velocity of ball element A and B in the normal unit vector at current time-step:

$$[\widetilde{\omega}_i] = \frac{1}{2}\left(\omega_{\mathrm{A}j} + \omega_{\mathrm{B}j}\right)n_j n_i (i = 1,\ 2,\ 3) \tag{24}$$

Finally, the contact force by elastic spring in tangential direction is as follows:

$$\left[E_i^s\right] = \left[E_i'^s\right] + \left[\Delta E_i^s\right](i = 1,\ 2,\ 3) \tag{25}$$

When the force by elastic spring in tangential direction $\left(\left[E_i^s\right]\right)$ surpasses the frictional force $\left(\mu.\left[E_i^n\right]\right)$, the force in tangential direction is set at $\mu.\left[E_i^n\right]$.

The viscous damping force in tangential direction is:

$$\left[D_i^s\right] = \eta^s \frac{\left[\Delta U_i^s\right]}{\Delta t}(i = 1,\ 2,\ 3) \tag{26}$$

Because the ball element in our numerical simulation has too much of an idealised round shape compared with the complex shape of the sand particles, it too much rotates in the numerical simulation by the distinct element method. Sakaguchi et al. (1993) took up the concept of rolling friction that was usually taken into consideration in the deformation of round-shaped objects such as tyres. Iwashita et al. (1995) set up the mechanical elements that allow the transmissions of the moment of contact points between disc elements in a two-dimensional distinct element method. Here, based on Iwashita's method, the rotational restraints were incorporated such that the rotational elastic spring and rotational viscous dashpot were placed between ball elements for the three-dimensional distinct element method (Fig. 1). The restraints by rotational elastic spring and rotational viscous dashpot are as follows:

$$\left\lfloor E_i^r\right\rfloor = K^r[\theta_{\mathrm{A}i}](i = 1,\ 2,\ 3) \tag{27}$$

$$\left\lfloor D_i^r\right\rfloor = \eta^r[\omega_{\mathrm{A}i}](i = 1,\ 2,\ 3) \tag{28}$$

where θ is rotation. Tests without rolling restraints do not take $\left\lfloor E_i^r\right\rfloor$ and $\left\lfloor D_i^r\right\rfloor$ into consideration. The forces acting on a ball element "A" with elastic spring and viscous damper by contacting neighbours (ball and wall elements) are the summation of those from all of contacting elements "B" as follows:

$$\left[\overline{E}_{\mathrm{A}i}\right] = \sum_{\mathrm{B}}[E_{\mathrm{B}i}](i = 1,\ 2,\ 3) \tag{29}$$

$$\left[\overline{D}_{\mathrm{A}i}\right] = \sum_{\mathrm{B}}[D_{\mathrm{B}i}](i = 1,\ 2,\ 3) \tag{30}$$

Finally, the equations of translational and rotational motion are as follows:

$$m_{\mathrm{A}}[\ddot{\chi}_{\mathrm{A}i}]_t = -\left[\overline{E}_i\right]_t - \left[\overline{D}_i\right]_t - [F_i]_t + m_{\mathrm{A}}[g_i] \tag{31}$$

$$I[\dot{\omega}_{\mathrm{A}i}]_t = -\varepsilon_{ijk}\left(\left\lfloor x_j^{(c)}\right\rfloor - \left[x_{\mathrm{A}j}\right]_t\right)\left(\left[\overline{E}_k\right]_t + \left[\overline{D}_k\right]_t\right) - \left\lfloor E_i^r\right\rfloor - \left\lfloor D_i^r\right\rfloor \tag{32}$$

By integrating these equations, velocity, position, and angular velocity are calculated as:

$$\begin{aligned}[\dot{\chi}_{\mathrm{A}i}]_{t+\Delta t_{/2}} &= [\dot{\chi}_{\mathrm{A}i}]_{t-\Delta t_{/2}} + [\ddot{\chi}_{\mathrm{A}t}]_t \cdot \Delta t,\ [\chi_{\mathrm{A}i}]_{t+\Delta t} \\ &= [\chi_{\mathrm{A}i}] + [\dot{\chi}_{\mathrm{A}i}]_{t+\Delta t_{/2}} \cdot \Delta t\end{aligned} \tag{33}$$

$$\begin{aligned}[\omega_{\mathrm{A}i}]_{t+\Delta t_{/2}} &= [\omega_{\mathrm{A}i}]_{t-\Delta t_{/2}} + [\dot{\omega}_{\mathrm{A}i}]_t \cdot \Delta t,\ [\theta_{\mathrm{A}i}]_{t+\Delta t} \\ &= [\theta_{\mathrm{A}i}]_t + [\omega_{\mathrm{A}i}]_{t+\Delta t_{/2}} \cdot \Delta t\end{aligned} \tag{34}$$

By using position $\left([\chi_{\mathrm{A}i}]_{t+\Delta t}\right)$, velocity $\left([\dot{\chi}_{\mathrm{A}i}]_{t+\Delta t_{/2}}\right)$, rotation $\left([\theta_{\mathrm{A}i}]_{t+\Delta t}\right)$, and angular velocity $\left([\omega_{\mathrm{A}i}]_{t+\Delta t_{/2}}\right)$, the values in the next time-step are calculated by repeating the procedures mentioned above.

Parameter determination

To attenuate the vibratory responses between ball and wall elements most rapidly and to reduce the calculation time, Cundall and Strack (1979) proposed a method, in which the viscous damping coefficient η^n was set at the critical damping coefficient (Eq. 35) in a one-dimensional mass-spring system (Eq. 36) described by a point mass m, elastic spring stiffness K^{n} and viscous damping coefficient (Kiyama and Fujimura 1983).

$$\eta_{\mathrm{crit}}^n = 2\sqrt{mk^n} \tag{35}$$

$$m\ddot{\chi} + \eta^n\dot{\chi} + K^n\chi = 0 \tag{36}$$

where η_{crit}^n is the critical damping coefficient. The elastic spring stiffness in tangential direction (k^s) is determined by introducing the taper rate s=0.25 based on Kiyama and Fujimura (1983) in considering the efficiency and reproduction of the results in the numerical simulations:

$$k^s = s \times \mathrm{K}^n \tag{37}$$

$$\eta^s = \sqrt{s} \times \eta^n \tag{38}$$

Uchida and Hakuno (1988), and Iwashita and Hakuno (1990) approximated the elastic spring stiffness in normal direction based on the elastic wave velocity in a one-dimensional mass-spring system. Kiyama and Fujimura (1983) and Tarumi and Hakuno (1987) determined the elastic spring stiffness in normal direction (K^{n}) by relating it to Young's modulus of soil particles by using the Heltz's contact theory. As the elastic spring stiffness set in the distinct element method might not agree with Young's modulus of the sand particle itself (Hakuno 1997), in this study, the elastic spring stiffness in normal direction was taken as the tuning parameter and set at $5.0\times10^{6.0}$ N/m. The coefficients of rotational spring and rotational dashpot were determined based on Iwashita and Hakuno (1990):

$$\mathrm{K}^r = k^s \times r^2, \eta^r = 0.001 \tag{39}$$

in which r is radius of ball element. The modulus of compressibility of water (E_w) is 2.1×10^9 Pa; however, Kiyama el al. (1994) and Hakuno and Tarumi (1988), respectively, set it at 2.0×10^6 Pa and 2.4×10^5 Pa to avoid too long calculation time and obtain the stable solutions in their simulations. In this study, the modulus of compressibility of water was set at 2.1×10^6 Pa. One time-step (Δt) was given by $\Delta t = \sqrt{\frac{m}{\mathrm{K}^n}}$. The particle friction coefficient was set at 0.6 (corresponding to 31° in friction angle) in that it related to the bulk internal friction angles usually found in the geo-technical soil tests on sands.

The numerical specimens were cylindrical in shape (0.10 m diameter and 0.20 m high) formed by three wall elements, i.e. a circumferential wall cylindrical in shape, upper end and lower end walls (Fig. 3). These wall elements were not deformed during the numerical simulation. The upper and lower end walls moved vertically, and the circumferential wall cylindrical in shape contracted or expanded radially. The ball elements had the uniform size of 0.015 m in diameter. The packing of the ball elements was conducted such that certain numbers of ball elements with a reduced diameter of 0.0031 m (0.625 times of 0.015 m) were created to effectively make assembly at the positions determined by the pseudo-random numbers within the cylindrical numerical space surrounded by wall elements. After that, the diameter of ball elements created within the wall elements was restored to 0.015 m to form the designated specimens. Initial confining stress of 20 kPa was given to normally (isotropic) consolidate the numerical specimens, then compressed with a constant axial speed of 0.01 m/sec (the upper end wall elements moved down vertically). The input parameters used are given in Table 1. The bulk permeability used in the simulation was the input value that was selected to be similar to the one found in the sandy soils. The bulk permeability was constant all through in the simulation, neglecting the changes in the void ratio in microscopic scale due to deformation of the assembly of ball elements during compression. Table 2 shows the identification number of numerical tests, void ratio when ball elements were packed within the cylindrical space before consolidation, initial void ratio (e_o) after consolidation, ball element number and conditions of rolling restraints.

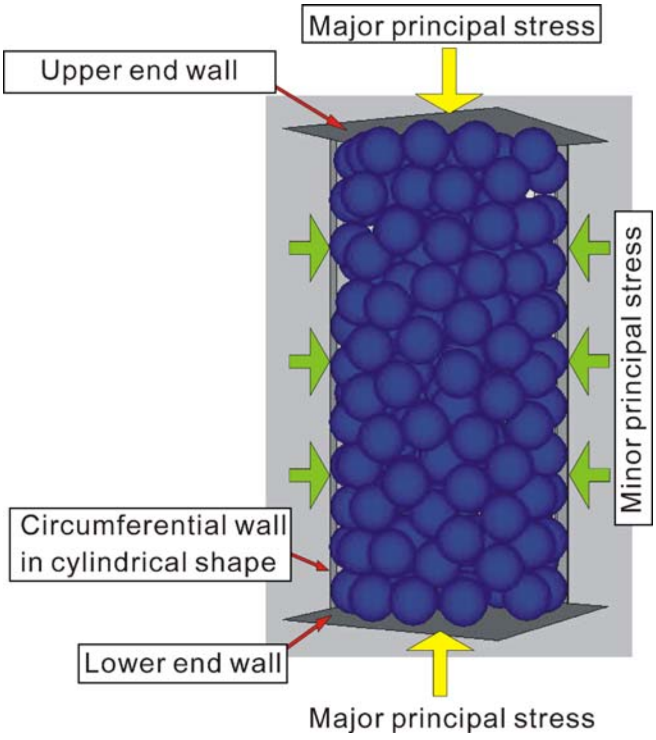

Fig. 3 Numerical specimen (ball and wall elements) for undrained triaxial compression test

Positive pore-water pressure build-up in loose numerical specimens

The liquefaction phenomenon is related to the contractive deformation under the undrained conditions, in which meta-stable loose structure collapses (Fig. 4a). The schematic illustration of the effective stress path when the liquefaction occurs is shown in Fig. 4b based on the results of triaxial compression tests (Vaid et al. 1989; Yamamuro and Lade 1998) and ring-type direct shear tests (Okada et al. 2000, 2004, 2005). The effective stress path should be going leftward associated with the positive pore-water pressure build-up; the shear resistance at the steady state is close to zero. The steady state was defined by Castro and Poulos (1977) and Poulos (1981) as that state in which effective mean stress, effective deviator stress and the volume of specimen reached constant values subjected to certain amount of displacement. Figure 5 shows the simulation results of triaxial compression test on loose numerical specimen (test 2). Just after the beginning of the test, the effective stress path went right–upward without the generation of positive pore-water pressure; after that it, it moved to the left due to the positive pore-water pressure build-up (Fig. 5a). Pore-water pressure and effective deviator stress $\left(q' = \frac{\sigma_1' - \sigma_3'}{2}\right)$ reached steady state at 1.5% axial strain (Fig. 5b). The final effective mean stress $p' = \frac{\sigma_1' + \sigma_3'}{2}$ at the steady state conditions was less than 25% of the initial value, leading to the production of quasi-liquefaction phenomenon. Test 1 at initial void ratio of 0.914 with rolling restraints, tests 9, 10 and 11 at initial void ratios of 0.914, 0.890 and 0.851 without rolling restraints, produced similar effective stress paths as that of test 2.

Results of medium and dense numerical specimens

In contrast to the loose specimens, the medium and dense specimens of sands tend to behave in the dilative manner in the undrained triaxial compression tests (Poulos 1981). Most dense specimens can produce even the negative pore-water pressure from the beginning in the undrained ring-type direct shear tests (Okada et al. 2000, 2004, 2005), as schematically shown in Fig. 6. The effective stress paths and the relationships of effective deviator stress and pore-water pressure vs axial strain of dense numerical specimen (test 8) are shown in Fig. 7. The effective stress path of dense numerical specimen first moved right–upward along the 45-degree line without the generation of positive pore-water pressure as was observed in test 2; however, the effective stress path swerved from the course to the right at 30 kPa of effective mean stress (Fig. 7a). The effective deviator stress generally increased its values monotonically with some minor fluctuations (Fig. 7b). Pore-water

Table 1 Input parameters for distinct element method

Parameter	Ball to ball	Ball to wall
Normal elastic spring stiffness, K^n	$5.00\times10^{6.0}$ N/m	$5.00\times10^{6.0}$ N/m
Tangential elastic spring stiffness, k^s	$1.25\times10^{6.0}$ N/m	0.0 N/m
Rotational elastic spring stiffness, K^r	$7.03\times10^{1.0}$ Nm	$7.03\times10^{1.0}$ Nm
Normal viscous damping coefficient, η^n	$2.27\times10^{5.0}$ Ns/m	$2.27\times10^{5.0}$ Ns/m
Tangential viscous damping coefficient, η^s	$1.13\times10^{5.0}$ Ns/m	$1.13\times10^{5.0}$ Ns/m
Rotational viscous damping coefficient, η^r	$1.00\times10^{-3.0}$ Nms	$1.00\times10^{-3.0}$ Nms
Parameter		
Coefficient of interparticle friction, $\tan\phi_\mu$	0.60	
Frictional coefficient of wall element	0.0	
Confining pressure, σ_3	2.00×10^{4} Pa	
Modulus of compressibility of water	$2.10\times10^{6.0}$ Pa	
Axial loading speed	$1.00\times10^{-2.0}$ m/s	
Bulk permeability	1.00×10^{-3} m/s	

pressure exhibited the positive values within the small range from the beginning to 0.25% of axial strain, then it monotonically decreased. Tests 6 and 7 with rolling restraints, and tests 13 and 14 without rolling restraints, produced quite similar results as that of test 8.

The effective stress path of medium numerical specimen (test 4) moved greatly to the left upto 7.5 kPa of effective mean stress, after the right–upward movement along the 45-degree line just after the beginning of the test (Fig. 8a). After reaching 7.5 kPa of effective mean stress, the effective stress path turned to a right–upward direction when both effective means stress and effective deviator stress tended to increase. The effective deviator stress exhibited a minimal value of 3.0 kPa at 3.8% axial strain, and then it increased to reach steady state (Fig. 8b). The pore-water pressure increased from the beginning of the test to reach peak (17.4 kPa) at 4.3% axial strain, then gradually decreased. This type of behaviour, i.e. positive pore-water pressure build-up due to the contractive deformation at the beginning of the test and the subsequent recovery of the effective mean stress associated with the reduction in generated pore-water pressure, was a typical characteristic of granular materials and defined as phase transformation (Alarcon-Guzman et al. 1988) or limited-liquefaction (Vaid et al. 1985). The effective stress path of test 4 confirmed that this phenomenon could be well reproduced in our numerical simulation.

To examine the undrained shear behaviour with rolling restraints of medium numerical specimens more in detail, test 3 and test 5, which were formed to be at close initial void ratio (e_o) to that of test 4 were conducted (void ratios upon creation and before consolidation were at 0.880 for test 3, 0.870 for test 4 and 0.860 for test 5, and e_o were at 0.873 for test 3, 0.867 for test 4 and 0.851 for test 5). The effective stress paths of test 3 and test 5 are shown in Fig. 9. The effective stress path of test 3 moved largely to the left, then at 3.8 kPa of effective mean stress, it turned right–upward to reach steady state, which also showed the phase transformation as found in test 4. The results of test 3 differed from test 4 in that the first left-shift of effective stress path was larger and the subsequent right–upward recovery was smaller in test 3 than those of test 4. This should be dependent on the slightly bigger initial void ratio of test 3 than that of test 4. The effective stress path of test 5, which was slightly denser than test 4 was similar to that of dense numerical specimen (test 8), in which the effective deviator stress monotonically increased. These results confirmed that the pore-water pressure behaviours were strongly associated with the slight differences in initial void ratios. The phase transformation

Table 2 Identification number of numerical tests and conditions

Test number	Void ratio when ball elements packed	Initial void ratio, e_0 after consolidation	Ball number	Rolling restraints	State
1	1.00	0.914	444	yes	Loose
2	0.900	0.890	467	yes	Loose
3	0.880	0.873	472	yes	Medium
4	0.870	0.867	475	yes	Medium
5	0.860	0.851	477	yes	Dense
6	0.850	0.850	480	yes	Dense
7	0.800	0.802	493	yes	Dense
8	0.750	0.766	507	yes	Dense
9	1.00	0.914	444	no	Loose
10	0.900	0.890	467	no	Loose
11	0.860	0.851	477	no	Loose
12	0.850	0.850	480	no	Medium
13	0.800	0.802	493	no	Dense
14	0.750	0.766	507	no	Dense

Loose, monotonic increase of pore-pressure, *Medium*, phase transformation, *Dense*, monotonic decrease of pore-pressure.

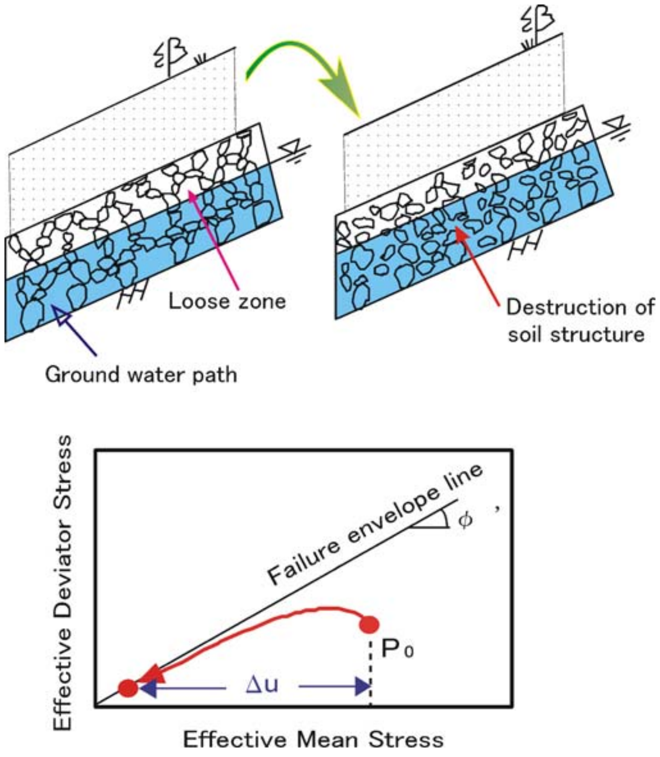

Fig. 4 Schematic illustration of **a** destruction of loose soil structure in liquefaction phenomenon and **b** effective stress path

behaviour was also observed in test 11 and 12 for tests without rolling restraints.

Examination of effective angle of internal friction (Φ')

Lambe and Whitman (1979) introduced a relationship of inter-particle friction angle (ϕ_μ) of quartz and the peak internal friction angles from geo-technical soil tests under drained conditions (ϕ_d) vs initial void ratio (e_o) (Fig. 10). The inter-particle friction angle of quartz was 26°, while the drained angles of internal friction (ϕ_d) were dependent on the initial void ratio. The smaller the initial void ratio, the larger the drained angle of internal friction. Castro and Poulos (1977) pointed out that the drained angles of internal friction at steady state, i.e. reaching a constant volume conditions, converged upon a constant value (ϕ_{cv}) irrespective of the initial void ratio. Casagrande (1936) schematically showed the void ratio within the shear zone that affected the angle of internal friction changed and converged upon a certain value at steady state, explaining the constant internal friction angle (ϕ_{cv}) from the specimens over the wide ranges of initial void ratio (Fig. 11). Roscoe and Schofield (1958) conducted simple shear tests on 1 mm steel balls confirming such concept. On the other hand, Fig. 10 showed that ϕ_{cv} exceeded ϕ_μ . This fact suggested that there was still some interlocking even when the steady state conditions was reached. Particles must still moved up and over their neighbours as straining proceeded, and on a scale equal to the particle size there, must be volume changes—both increases and decreases. The local effects combined in such a way that there was no volume change for the specimen of sands as a whole (Lambe and Whitman 1979).

Matsuoka (1974) mentioned that the bulk internal friction angle derived from the drained soil tests was the result of the combination of inter-particle friction angle (ϕ_μ) and the inter-locking effects between the neighbouring particles (Fig. 12). Substituting the average slope (θ_{av}) for the inter-locking angle of each soil particle at contact point (θ_i), the frictional coefficient (the ratio of shear stress to normal stress) is expressed as:

$$\frac{\tau}{\sigma} = \tan\left(\phi_\mu + \theta_{av}\right)$$

In this study, the coefficient of inter-particle friction ($\tan\phi_\mu$) was set at 0.6 (corresponding to 31° of friction angle) in consid-

Fig. 5 Results of undrained triaxial compression test on loose numerical specimen: **a** effective stress path; and **b** relationship between effective deviator stress and pore-water pressure and axial strain

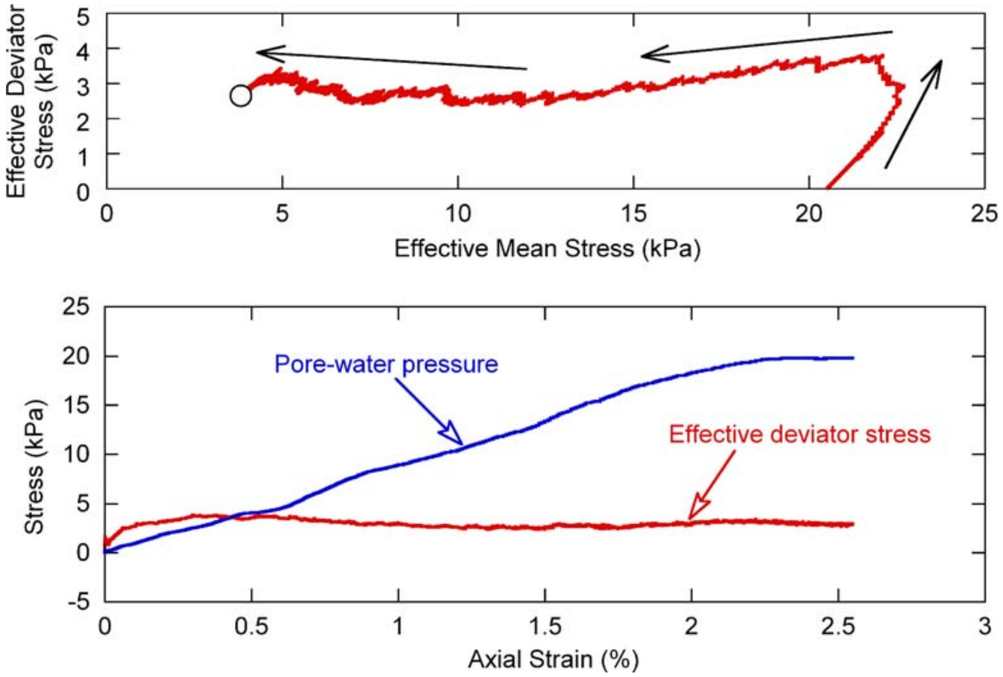

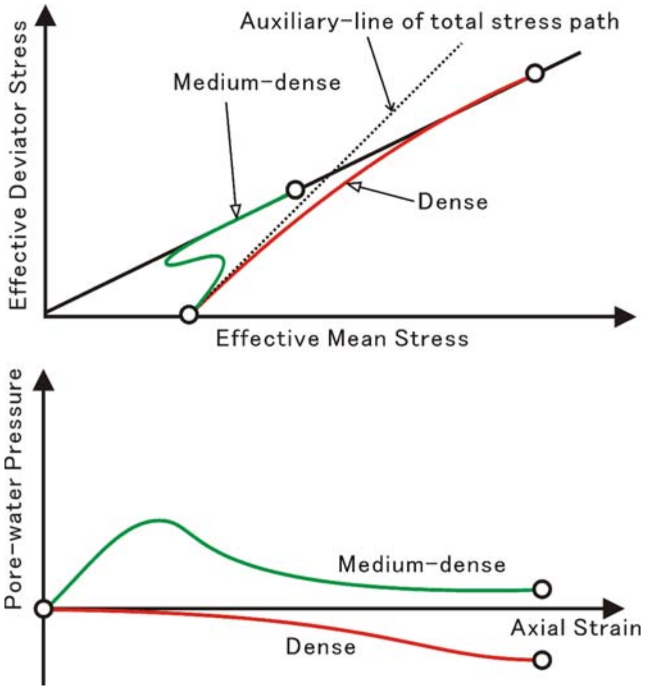

Fig. 6 Schematic illustration of **a** effective stress paths and **b** relationship between effective deviator stress and pore-water pressure vs axial strain of medium-dense and dense specimens

eration of the bulk internal friction angle generally mobilised in the geo-technical soil tests on sands. Figure 13 showed the relationship between mobilised peak effective angles of internal friction (ϕ'_p) and the initial void ratios (e_o; also Table 3 listed the peak effective angle of internal friction). Tests 2 and 3 with rotational restraints and tests 9 and 10 without rolling restraints produced too large peak effective angles of internal friction that were larger than 40°. This was likely because the stress points that mobilised peak effective angles of internal friction in these tests were located at the ranges of small effective mean stress on a stress plane, in which large positive pore-water pressure were produced. When the effective mean stresses were small on a stress plane, the effective angles of internal friction largely changed their values associated with the small changes in effective mean stress due to the positive pore-water pressure build-up. As for test 1, which also produced large positive pore-water pressure, the peak effective angle of internal friction was 27.9°. These problems should be solved by generating large numbers of ball elements and calculating the fluid-flows between neighbouring measurement spheres in higher resolutions in the cylindrical shaped numerical specimens, in which the stress states should be more similar to the real conditions in the undrained triaxial compression tests on sands.

As for the tests with negative pore-water pressure generation (tests 5, 6, 7 and 8 with rolling restraints, tests 12, 13 and 14 without rolling restraints), it was found that the specimens at a smaller initial void ratio produced larger peak effective angles of internal friction, and this agreed with the facts that the strong interlocking

Fig. 7 Results of undrained triaxial compression test on dense numerical specimen: **a** effective stress path; and **b** relationship between effective deviator stress and pore-water pressure and axial strain

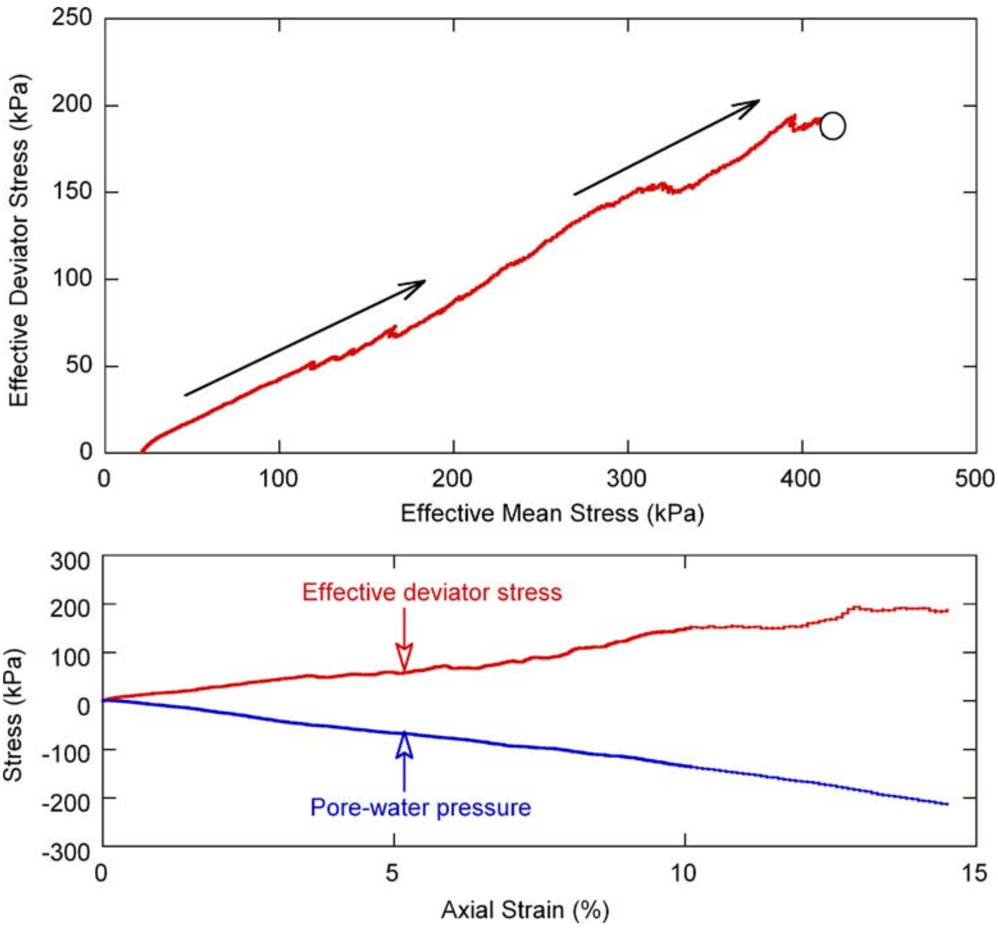

Fig. 8 Results of undrained tri-axial compression test on medium-dense numerical specimen: **a** effective stress path; and **b** relationship between effective deviator stress and pore-water pressure and axial strain

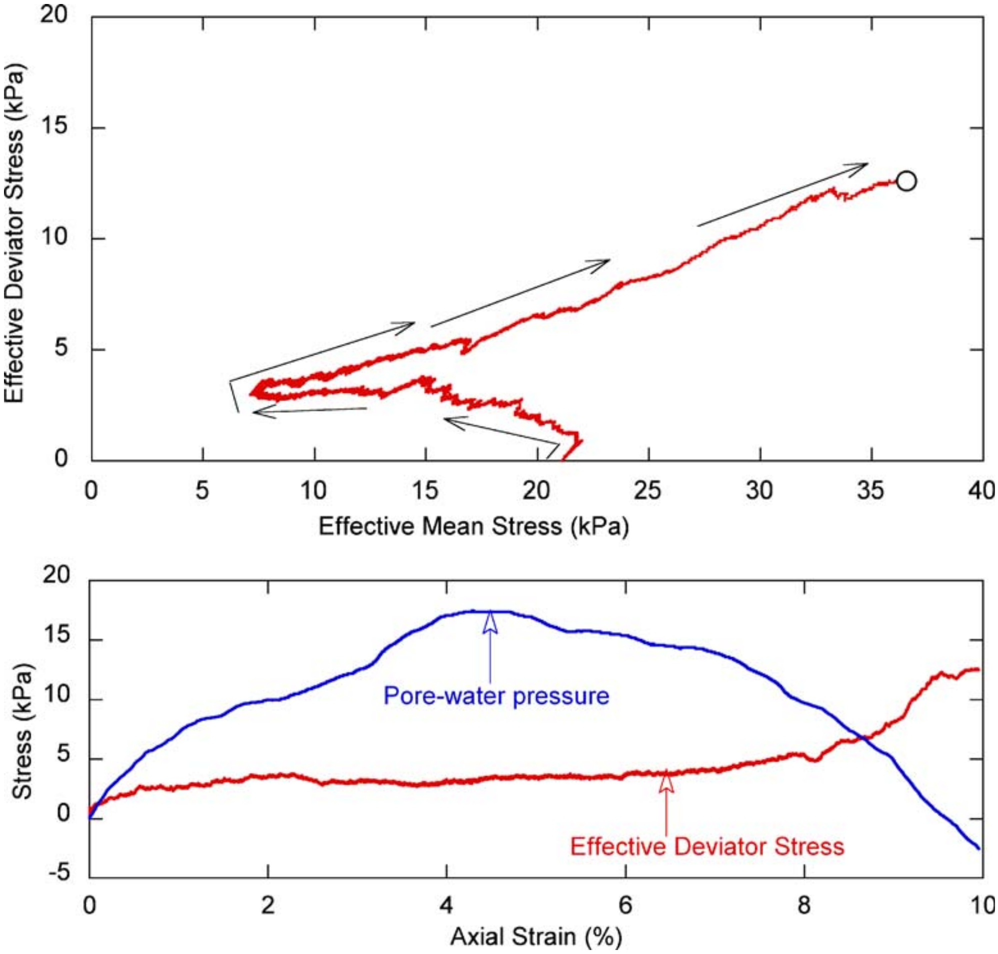

Fig. 9 Effective stress paths of medium-dense numerical specimens (tests 3 and 5)

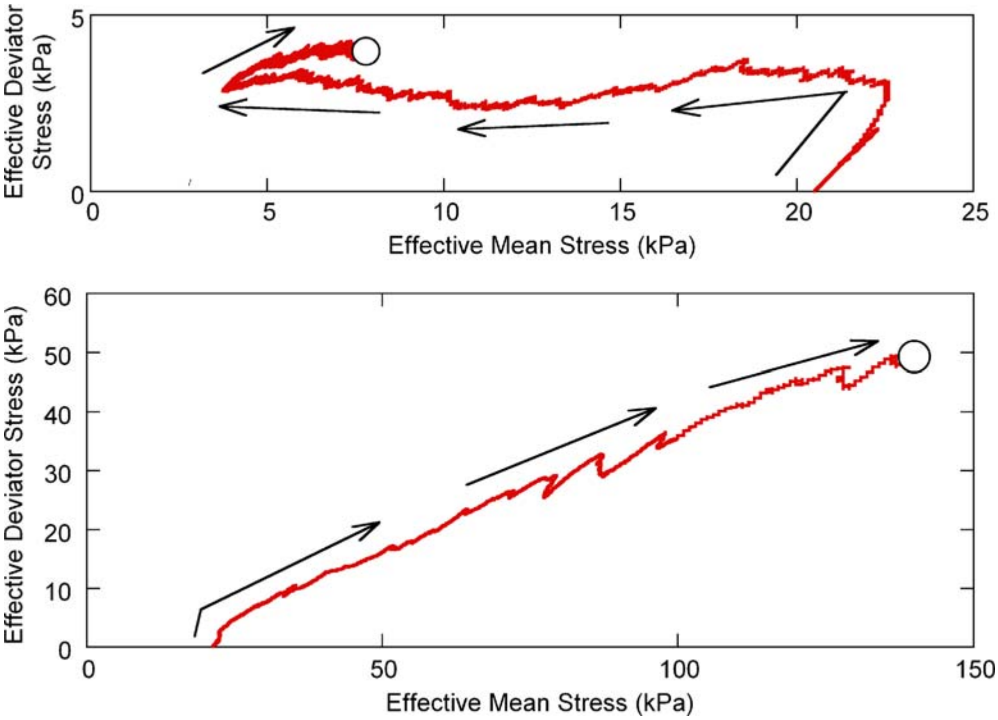

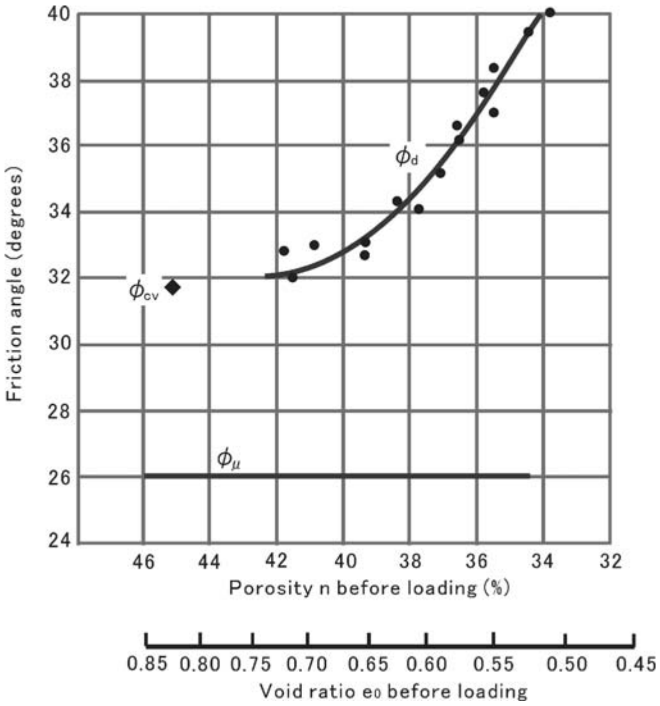

Fig. 10 Relationship between inter-particle friction angle (ϕ_μ), angle of internal friction at steady state (φ_{cv}), and drained angle of internal friction (φ_d) versus porosity (after Lambe and Whitman 1979)

in the denser specimens yielded the larger peak effective angles of internal friction as shown in Fig. 10. It should be mentioned that the data of Lambe and Whitman (1979) were drained angles of internal friction (ϕ_d) and they were different from peak effective angles of internal friction (ϕ'_p) obtained in our numerical simulations. However, the Japanese Geotechnical Society (1985) stated that ϕ'_p obtained in the effective stress analysis on soils was generally close to ϕ_d. Accordingly, the difference between ϕ_d and ϕ'_p was neglected in the discussion. The mobilised peak effective angles of internal friction were smaller than 31° set for the simulation parameter as inter-particle friction angle, except for tests 2 and 3 with rolling restraints and tests 9 and 10 without rolling restraints (see Fig. 13). Based on Matsuoka's explanation, the peak effective angle of internal friction should be larger than the inter-particle friction angle; however, the obtained results showed the opposite. This was likely attributable to two facts: (1) the soil particles, in general, have quite complex shapes forming the very complicated skeletal structures within soil layers. On the other hand, only very simple structures can be constructed by the idealised round-shape ball elements in our numerical simulation, resulting in quite different structures from the real complicated ones; and (2) real soils have particles in wide varieties of sizes; however, in our numerical simulation, the particles with uniform size were used. To simulate the values of effective angle of internal friction, further studies from these viewpoints are necessary. From Fig. 13, it was confirmed that the rotational restraints had slight effects in increasing the peak effective angles of internal friction of tests 6, 7 and 8 that produced negative pore-water pressure in comparison with tests without rotational restraints at the same void ratios (tests 12, 13 and 14). However, it was not sufficient to reproduce the desirable values of effective angle of internal friction. As for tests with positive pore-water pressure (tests 1, 2, 3, 4, 9 and 10), the clear effects of rotational restraints on peak effective angle of internal friction were not confirmed.

Steady state strengths and initial void ratios

The steady state line was defined on an effective deviator stress (or effective mean stress) at steady state–initial void ratio diagram by triaxial compression tests (Castro and Poulos 1977; Poulos 1981), in which the specimens positioning above this line should be contractive and below it, dilative in the undrained tests. Been and Jefferies (1985) proposed the state parameter evaluating the liquefaction potential in that the distance from the initial point of a specimen to the steady state line before shearing after consolidation expressed the potential. Okada et al. (2000) examined the positions of the steady state lines derived from the two different types of soil tests, i.e. triaxial compression tests and ring-type

Fig. 11 Changes in void ratio within shear zone during shearing (after Casagrande 1936)

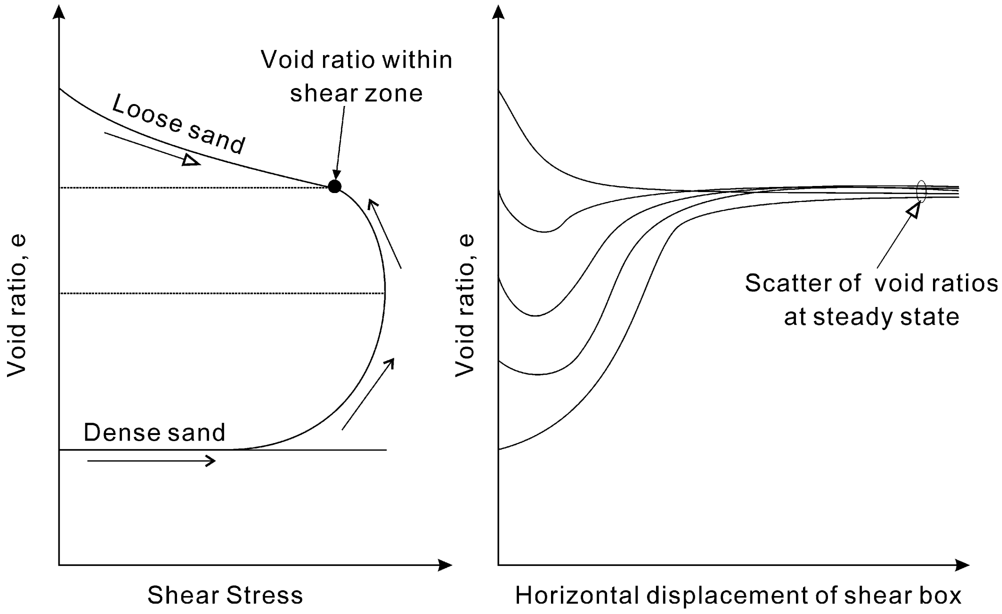

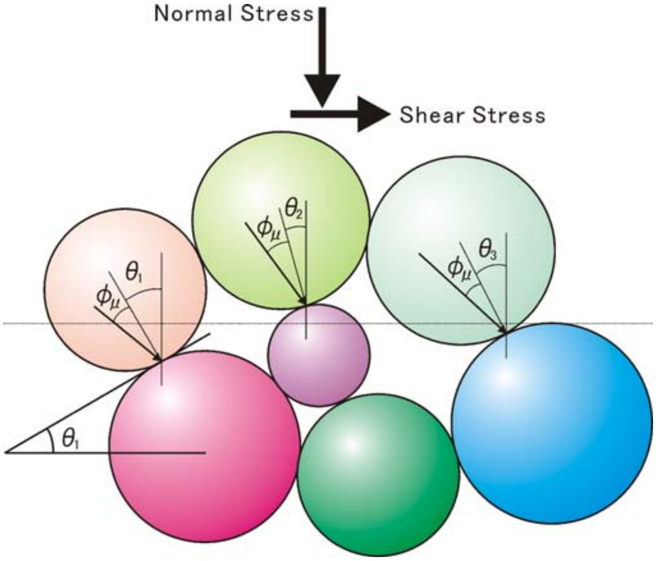

Fig. 12 Schematic illustration of frictional coefficient related to interparticle friction angle and interlocking (after Matsuoka 1974)

direct shear tests on two kinds of sand. It was shown that the ring-type direct shear tests produced smaller steady state strengths for the medium-dense through dense specimens than those of triaxial compression tests mainly due to the particle crushing effects.

Figure 14 shows the relationship of ball numbers in the specimens and effective deviator stress at steady state vs initial void ratio (Table 3 also listed the effective deviator stress at steady state). The ball numbers in the specimens and the initial void ratio had a linear relationship except for test 1 (Fig. 14a). In test 1, the numbers of ball element initially created to be 1.00 void ratio before consolidation was too small, then the initial consolidation of 20 kPa confining stress largely shrunk the specimen to be 0.914 of initial void ratio.

As for the tests without rolling restraints, the effective deviator stresses at a steady state of tests 12, 13 and 14, which produced negative pore-water pressure were almost on a straight line (SSL-1) proportional negatively to initial void ratio (Fig. 14b), agreeing well with the steady state line concept. However, test 11 at almost the same initial void ratio as test 12 suddenly produced a small effective deviator stress at steady state as found in tests 9 and 10. Hence, this result implied that a critical void ratio above which the quasi-liquefaction was produced and below which no quasi-liquefaction was, may exist. However, this result did not agree with the one from the real soils. On the contrary, as for the tests with rotational restraints, also a straight line could be found for tests 3, 4, 5, 6, 7 and 8 (SSL-2), just above the SSL-1, although the effective deviator stresses at steady state from tests 1 and 2 that reproduced the quasi-liquefaction were not on SSL-2. The effective deviator stresses of test 3 (e_0=0.873) and test 4 (e_0=0.867) narrowed the gap between the quasi-liquefaction and no quasi-liquefaction divided by the critical void ratio found in the tests without rotational restrains. Although the points of loose numerical specimens did not lie on the steady state line, the relationship between the effective deviator stress–initial void ratio from the tests with rotational restraints turned into the plots similar to that of the real soils. The rotational restraints were not so effective for the increase in effective angle of internal friction; however, they played an important role in the changes in volumetric strain and the subsequent pore-water pressure generation especially in test 3 and test 4 to make the results more similar to the real one. The difference of results from the real soil tests and numerical simulations are likely attributable to the shape of particles. The simple structure with idealised ball elements in our numerical simulation produced large positive pore-water pressure resulting in quasi-liquefaction, if the void ratios were larger than a certain value and the results converged to be almost the same. On the contrary, the complicated skeletal structure with complex shaped real soil particles were strongly to be influenced with the slight differences in void ratio for the movements of soil particles followed by the different pore-water pressure behaviour.

Concluding remarks

Pore-water pressure was coupled with three-dimensional distinct element method, in which the changes in pore-water pressure in the undrained triaxial compression tests were numerically reproduced. The values of effective angles of internal friction obtained from our numerical simulations did not agree well with the values of the real soils. It was assumed that the increment of the numbers of ball element and the specimens with particles in

Fig. 13 Observed peak effective angles of internal friction vs initial void ratio (e_0)

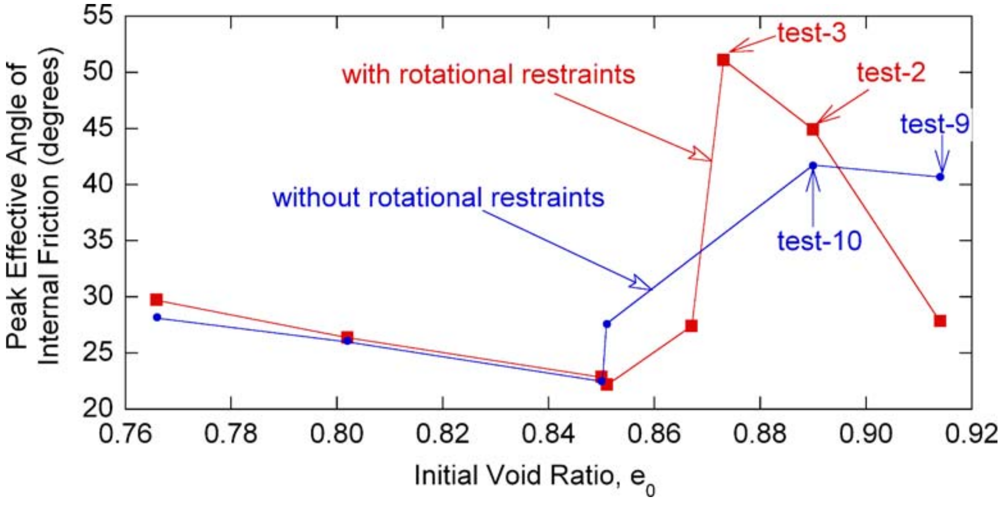

Table 3 Peak effective angles of internal friction and effective deviator stress at steady state

Test number	Peak effective angle of internal friction	Effective deviator stress at steady state
1	27.9	3.610
2	44.9	2.774
3	51.1	3.698
4	27.4	12.25
5	22.2	47.14
6	22.9	48.62
7	26.4	115.1
8	29.8	189.4
9	39.2	3.269
10	41.7	2.845
11	25.8	3.215
12	20.0	33.64
13	20.6	106.7
14	27.0	179.8

different sizes and shapes were necessary. The results of our numerical simulation of undrained triaxial compression tests were for the certain element within the landslide mass. However, it must be important for the basic contributions to the elucidation of the fluidisation mechanisms of the flow-type landslides, especially caused by earthquakes, which frequently produced liquefaction-induced geo-disasters.

- Pore-water pressure was coupled with distinct element method by introducing the measurement sphere. Pore-water pressure assigned to the measurement spheres was calculated by the products of volumetric strain and modulus of compressibility of water, and it reproduced well the quasi-liquefaction behaviour in loose numerical specimens and the phase transformation behaviour in medium-dense numerical specimens.
- The effective angles of internal friction of the numerical specimens that produced negative pore-water pressure tended to increase with decreasing initial void ratio. This agreed well with the fact that the larger angles of internal friction will be generated in the denser specimens with stronger inter-locking.
- The steady state line on effective deviator stress–initial void ratio diagram could be found only in the tests that produced negative pore-water pressure. The points of the numerical specimens that produced positive pore-water pressure was not on that line. The results of tests without rotational restraints exhibited the gap between quasi-liquefaction and no quasi-liquefaction states; however, the results of tests with rotational restraints rather narrowed that gap resembling the results from the real soils better. The rotational restraints did not largely affect the effective

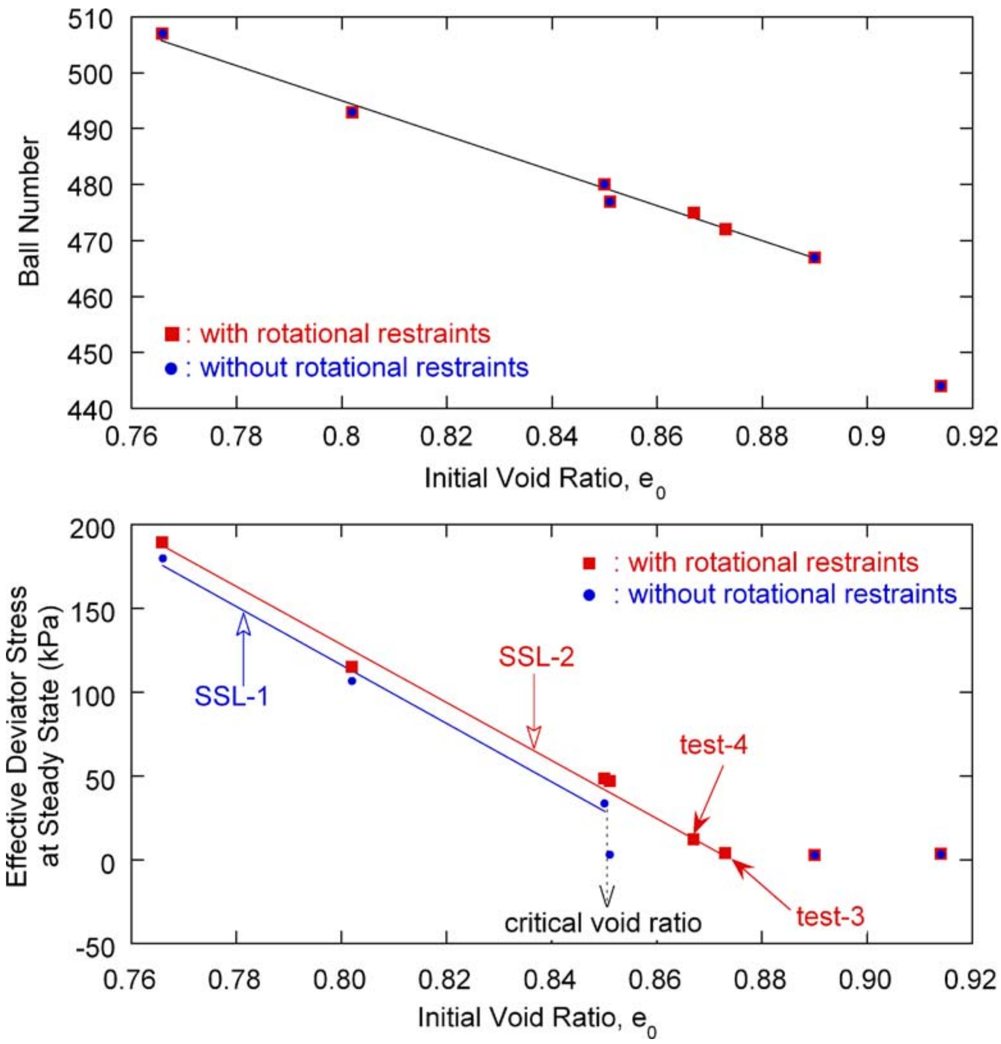

Fig. 14 Relationship between initial void ratio (e_0) and **a** ball element numbers and **b** effective deviator stress at steady state

angle of internal friction but played an important role in the changes in volume changes and the subsequent pore-water pressure behaviour.

Acknowledgements

The late Dr Okura (former Forestry and Forest Products Research Institute) played the major role in modeling of fluid-coupling in distinct element method. The authors dedicate this paper to Dr Okura. The authors wish to thank Prof. Y. Shimizu of Tokai University for his valuable suggestions for the improvements of source code. Sincere thanks are due to Dr P. Cundall of Itasca Consulting Group, Inc. for providing very fruitful discussion.

References

Alarcon-Guzman A, Leonards GA, Chameau JL (1988) Undrained monotonic and cyclic strength of sands. ASCE J Geotech Geoenviron Eng Div 114(10):1089–1109

Been K, Jefferies MG (1985) A state parameter for sands. Géotechnique 35(2):99–112

Casagrande A (1936) Characteristics of cohesionless soils affecting the stability of slopes and earth fills. J Boston Soc Civ Eng 23(1):13–32

Casagrande A (1971) On liquefaction phenomenon. Géotechnique 21(3):197–202

Castro G, Poulos SJ (1977) Factors affecting liquefaction and cyclic mobility. ASCE J Geotech Geoenviron Eng Div 103(GT6):501–516

Cundall PA (1989) Distinct element models of rock and soil structure. In: Brown ET (ed) Analytical and computational methods in engineering rock mechanics. Allen & Unwin, London, pp 129–163

Cundall PA, Strack ODL (1979) A discrete numerical model for granular assemblies. Géotechnique 29(1):47–65

Eckersley JD (1985) Flowslides in stockpiled coal. Eng Geol 22:13–22

Finn WDL (1981) Liquefaction potential: developments since 1976. In: Proceedings of the 1st International Conference on Recent Advances in Geotechnical Earthquake Engineering and Soil Dynamics. University of Missouri-Rolla, Roll, 2:655–681

Hakuno M (1997) Numerical simulation for failures. Morikita, Tokyo (in Japanese)

Hakuno M, Tarumi Y (1988) A granular assembly simulation for the seismic liquefaction of sand. In: Proceedings of Japan Society of Civil Engineers. 398(1–10):129–138

Hutchinson JN (1986) A sliding-consolidation model for flow slides. Can Geotech J 32:610–623

Ishihara K (1993) Liquefaction and flow failure during earthquakes. Géotechnique 43 (3):351–415

Ishihara K, Okusa S, Oyagi N, Ischuk A (1990) Liquefaction-induced flowslide in the collapsible loess deposit in Soviet Tajik. Soil Found 30(4):73–89

Iverson RM, LaHusen RG (1989) Dynamic pore-pressure fluctuations in rapidly shearing granular materials. Science 246:796–799

Iwashita K, Hakuno M (1990) Modified distinct elements method simulation of dynamic cliff collapses. In: Proceedings of Japan Society of Civil Engineers. 416(I–13):145–154 (in Japanese)

Iwashita K, Matsuura K, Oda M (1995) Distinct element method with the effect of moment transfer at the contact points. In: Proceedings of the Japan Society of Civil Engineers. 529(III–33):145–154 (in Japanese with English abstract)

Kiyama H, Fujimura H (1983) Application of Cundall's discrete block method to gravity flow analysis of rock-like granular materials. In: Proceedings of the Japan Society of Civil Engineers. 333:137-146 (in Japanese with English abstract)

Kiyama H, Nishimura T, Fujimura H (1994) An advanced distinct element model coupling with pore water. In: Proceedings of the Japan Society of Civil Engineers. 499:31–39 (in Japanese with English abstract)

Lambe TW, Whitman RV (1979) Soil Mechanics SI version. Wiley, New York, p 553

Matsuoka H (1974) Stress-strain relationships of sands based on the mobilized planed. Soil Found 14(2):47–61

Ng TT, Dobry R (1994) Numerical simulations of monotonic and cyclic loading of granular soils. ASCE J Geotech Geoenviron Eng Div 120(2):388–403

Okada Y, Ochiai H (2006) Simulating undrained triaxial compression behaviour by fluid-coupled distinct element method. In: Marui H, Marutani T, Watanabe N, Kawabe H, Gonda Y, Kimura M, Ochiai H, Ogawa K, Fiebiger G, Heumader J, Rudolf-Miklau F, Kienholz H, Mikos M (eds) (2006) Proceedings of the INTERPRAEVENT International Symposium, Disaster mitigation of debris flows, slope failures and landslides, Universal Academy Press, Tokyo, pp 447–453

Okada Y, Sassa K, Fukuoka H (2000) Liquefaction and the steady state of weathered granitic sands obtained by undrained ring shear tests: a fundamental study of the mechanism of liquidized landslides. J Nat Disaster Sci 22(2):75–85

Okada Y, Sassa K, Fukuoka H (2004) Excess pore pressure and grain crushing of sands by means of undrained and naturally drained ring-shear tests. Eng Geol 75:325–343

Okada Y, Sassa K, Fukuoka H (2005) Undrained shear behaviour of sands subjected to large shear displacement and estimation of excess pore-pressure generation from drained ring shear tests. Can Geotech J 42(3):787–803

Okura Y, Sammori T, Ochiai H (1994) Numerical analysis of debris movement within a landslide by distinct element method. Journal of the Japan Society of Erosion Control Engineering 47(3):3–10 (in Japanese with English abstract)

Okura Y, Ochiai H, Cundall PA, Shimizu Y (2004) Fluid coupling in PFC^{3D} using the measurement spheres. In: Shimizu Y, Hart R, Cundall P (eds) (2004) Proceedings of the 2nd International PFC Symposium on Numerical Modeling in Micromechanics via Particle Method-2004, AA Balkema, London, pp 257–264

Poulos SJ (1981) The steady state deformation. ASCE J Geotech Geoenviron Eng Div 107 (GT5):553–562

Roscoe KH, Schofield AN (1958) On the yielding of soils. Géotechnique 7:25–53

Sakaguchi H, Ozaki E, Igarashi T (1993) Plugging of the flow of granular materials during the discharge from a silo. Int J Mod Phys B 7:1949–1963

Sassa K (1988) Motion of landslides and debris flows—prediction of hazard area. In: Report of Grant-in-Aid for Scientific Research by Japanese Ministry of Education, Science and Culture

Sassa K (1996) Prediction of earthquake induced landslides, Special Lecture of 7th International Symposium on Landslides. Landslides, Balkema ,Vol.1, pp 115–132

Sassa K, Fukuoka H, Scarascia-Mugnozza G, Evans S (1996) Earthquake-induced-landslides: Distribution, motion and mechanisms. Special Issue for the great Hanshin Earthquake Disasters. Soil Found, Special Issue 53–64

Seed HB (1979) Soil liquefaction and cyclic mobility evaluation for level ground during earthquakes. ASCE J Geotech Geoenviron Eng Div 105:201–255

Seed HB, Lee KL (1966) Liquefaction of saturated sand during cyclic loading. ASCE Journal of the Soil Mechanics and Foundations Division 92(CM6):105–134

Tarumi Y, Hakuno M (1987) A granular assembly simulation for the liquefaction of sand and quicksand. In: Bulletin of Earthquake Research Institute, University of Tokyo. 62:535–577 (in Japanese with English abstract)

The Japanese Geotechnical Society (1985) Glossary for geotechnical engineering. The Japanese Geotechnical Society, Tokyo (in Japanese)

Uchida Y, Hakuno M (1988) Analysis of dry rock avalanches and debris flows by granular assembly simulation. In: Bulletin of Earthquake Research Institute, University of Tokyo. 65:321–411

Vaid YP, Chern JC, Tumi H (1985) Confining pressure, grain angularity, and liquefaction. ASCE J Geotech Geoenviron Eng Div 111(10):1229–1235

Vaid YP, Chung EKF, Kuerbuis RH (1989) Stress path and steady state. Can Geotech J 27:1–7

Yamamuro JA, Lade PJ (1998) Steady-state concepts and static liquefaction of silty sands. ASCE J Geotech Geoenviron Eng Div 124(9):868–878

Yoshimi Y, Richart FE, Prakash S, Balkan DD, Ilyichev VA (1977) Soil dynamics and its application to foundation engineering. In: Proceedings of 9th International Conference on Soil Mechanics and Foundation Engineering. Balkema, Rotterdam, vol. 2, pp 605–650

Y. Okada (✉) · H. Ochiai
Incorporated Administrative Agency, Forestry and Forest Products Research Institute,
305-8687 Matsunosato 1,
Tsukuba, Ibaraki, Japan
e-mail: okada10@ffpri.affrc.go.jp